Malcolm Macdonald
United Technologies Research Center,
411 Silver Lane,
East Hartford, CT 06108
e-mail: macdonm1@utrc.utc.com

S. Ravi Annapragada
United Technologies Research Center,
411 Silver Lane,
East Hartford, CT 06108
e-mail: annaprs@utrc.utc.com

Aritra Sur
United Technologies Research Center,
411 Silver Lane,
East Hartford, CT 06108
e-mail: sura@utrc.utc.com

Reza Mahmoudi
United Technologies Research Center,
411 Silver Lane,
East Hartford, CT 06108
e-mail: MAHMOURE@utrc.utc.com

Charles Lents
United Technologies Research Center,
411 Silver Lane,
East Hartford, CT 06108
e-mail: LentsCE@utrc.utc.com

Ankur Jain
Department of Mechanical and Aerospace Engineering,
University of Texas at Arlington,
Arlington, TX 76019
e-mail: jaina@uta.edu

Early Design Stage Evaluation of Thermal Performance of Battery Heat Acquisition System of a Hybrid Electric Aircraft

The electric energy and power storage, conversion and distribution (ESC&D) system of a hybrid electric aircraft, even at high efficiency, will reject significant heat at relatively low temperature. Thermal management systems (TMSs) can add excessive weight (heat exchangers and pumps) and impose excessive parasitic power consumption (pumps and fans) and drag (engine fan stream air and ram air) on the aircraft. Thus, effective low-weight thermal management of the ESC&D system is critical to realizing the potential benefits of a hybrid electric aircraft. This paper carries out early design stage benchmarking and evaluation of various thermal management approaches for the battery heat acquisition system of a hybrid electric aircraft. It is shown that the battery heat acquisition system based on state-of-the-art automotive electric vehicle design may be a third of the weight of the battery itself. Alternative approaches discussed here have the promise of reducing this weight by more than 60%. [DOI: 10.1115/1.4046159]

Keywords: hybrid electric aircraft, lithium-ion battery safety, thermal management, thermal runaway, analysis and design of components

1 Introduction

With the motivation of reducing carbon emissions by 50% by the year 2050, a significant amount of attention has been focused on technologies to reduce aircraft emissions. Electric-based aircraft propulsion is a key area of interest in this direction [1–3]. Both completely electric as well as hybrid configurations have been investigated [4,5]. Compared to traditional, fuel-based propulsion, electric propulsion may offer improved mission design flexibility and other strategic advantages [4]. However, several key technological challenges in electric flight remain to be fully addressed.

A typical electrical propulsion system comprises an electric drive train and an electric energy and power storage, conversion and distribution (ESC&D) system [1,6]. The ESC&D system of a hybrid electric aircraft, even at high efficiency, is expected to reject a significant amount of low-grade heat. As a result, effective thermal management of the ESC&D system is a critical technological challenge. Depending on its nature, however, a thermal management system can add excessive weight and impose significant parasitic power consumption. In the specific case of aircraft propulsion, increased drag due to the use of engine fan stream air and ram air by the thermal management system is also a key concern. These thermal management related concerns must be clearly addressed for optimizing the performance of hybrid electric propulsion.

Several prototypes of fully electric aircraft have been developed in the recent past, and multiple approaches for hybrid aircraft propulsion are also being investigated [4]. Recent work indicates that around 1000 W-h/kg energy storage may be required for hybrid electric flight to be economically feasible when compared to traditional jet propulsion [3]. A recently proposed 5-MW parallel hybrid configuration [1] provides a representative set of thermal management requirements. In this case, the ESC&D system comprises a 2029 kW-h battery system, two 2.2 MW motor drives, two 2.1 MW motors, and the associated power panels and feeders. Such a system will require the battery system to provide 2.5 MW of power to drive the motor. Based on the relatively high gravimetric energy density, higher cycle lifetime, and low self-discharge, Li-ion batteries offer the strongest potential as a candidate for the required energy storage requirements [6]. However, even when operating at relatively high efficiency of around 95%, the heat generated from the battery is estimated at around 125 kW. Current lithium-ion battery technology has a desirable operating temperature range of between 10 °C and 40 °C, which means heat is also rejected at these low-grade temperatures. Moreover, the heat sink temperature (air) ranges between 50 °C on a hot day and 0 °C at 30,000 ft. This combination of a large quantity of heat that must be rejected and the comparable temperatures of the source and sink would typically result in large heat exchangers, and excessive additional weight. The efficient design for the battery heat acquisition system (BHAS) for such aircrafts is clearly very important, as it would directly impact battery safety and reliability as well as contribute to the overall weight of the propulsion system.

Manuscript received August 14, 2019; final manuscript received January 16, 2020; published online January 29, 2020. Assoc. Editor: George Nelson.

While Li-ion batteries offer several advantages as outlined earlier, there are also several associated challenges. The performance and reliability of Li-ion batteries are highly temperature dependent [7,8]. Capacity fade, power fade, and self-discharge at high operating and shelf temperatures are well known [8]. Beyond a threshold temperature, thermal runaway can be triggered, which causes catastrophic failure [9]. These are all critical concerns in the context of electric flight, and therefore, effective dissipation of the generated heat during operation of Li-ion batteries is necessary to ensure compatibility with the tight standards of safety and reliability associated with flight. Thermal management of Li-ion batteries and battery packs for high power applications has received significant attention in the recent past. A variety of battery heat acquisition (BHA) systems have been proposed at multiple scales from a single cell to a fully packaged battery pack [7,10]. Air and water cooling, phase-change cooling, heat pipe-based cooling, etc. have been investigated [10]. Geometric optimization of battery packs has been carried out [11] although not in the context of electric flight. On the other hand, the management of heat generation in electrodes and improved material and interfacial thermal transport within the cell have also been investigated [12].

It is important to benchmark and compare the various approaches for battery thermal management summarized earlier in the context of cooling of a battery pack for electric flight. The ideal thermal management approach for electric flight must adhere to several challenges unique to flight. For example, while a stream of ram air is readily available to be used as a coolant, on the other hand, minimizing the total weight and additional power consumed by the thermal management system is extremely important in order to reduce additional fuel burn due to BHA system's weight. Despite the significant literature available on various candidate thermal management approaches for batteries, detailed considerations for the design of such a BHA system for hybrid electric aircrafts in the literature is lacking. There is also a distinct lack of benchmarking and performance comparison across candidate approaches that may help determine the appropriate technology to be used for hybrid electric flight. Any such benchmarking framework must account for the unique heat transfer aspects of Li-ion cells, such as anisotropic thermal conductivity [13] and extreme temperature sensitivity, as well as constraints unique to flight, such as those summarized earlier.

This paper reports research on system-level design and analysis of thermal management of a battery pack for hybrid electric flight. A modeling framework is presented that helps optimize thermal management for the least weight and highest performance for acquiring cell-level battery heat with a coolant supplied by the broader aircraft thermal management system. A steady-state analysis of heat transfer from within the cell all the way to the ultimate thermal sink is carried out. This approach offers a framework for comparison of candidate thermal management technologies, as well as optimization of the Li-ion cells themselves with the specific goal of reducing fuel burn. Results indicate that the baseline BHA system is approximately a third of the weight of the battery cells themselves, thus significantly adding to the overall system weight. Potential approaches for reducing this weight by more than 60% are discussed. These results contribute toward early-stage design tools for benchmarking and optimizing the performance of candidate thermal management approaches for hybrid electric flight.

2 Cell Thermal Model

A one-dimensional steady-state heat transfer model is developed in order to determine the cell temperature rise and understand the role of various thermal resistances in the path of heat flow from within the cell all the way to the ambient. This early-stage design tool helps quantify the thermal performance of various thermal management approaches for cooling the battery of a hybrid electric aircraft. The steady-state approach used in this work is appropriate

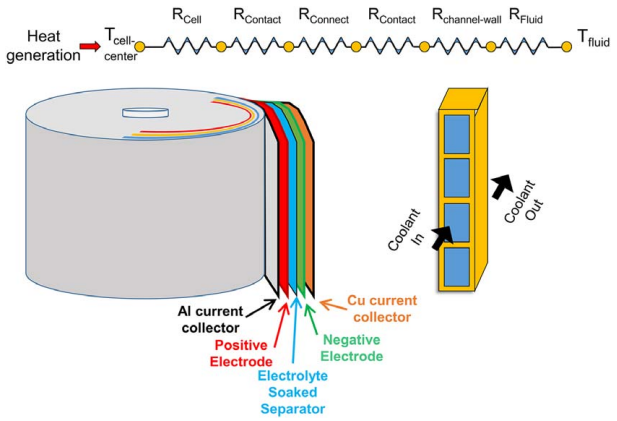

Fig. 1 1D Heat transfer modeling framework

for early-stage design analysis and benchmarking, as the steady-state analysis is much faster than transient analysis, while it also captures the essential thermal characteristics of the system. The thermal resistance-based model is shown in Fig. 1. A cylindrical 18650 cell—one of the most commonly used configurations—is assumed as a baseline. The coolant flows adjacent to the outer surface of the cell casing through a flow channel. Heat is assumed to be generated in the cell and flow radially outward toward the solid–fluid interface of the flow channel, from where it is carried away by the fluid. A constant 2C discharge rate is assumed, which, based on past measurements on Li-ion cells [14], corresponds to a volumetric heat generation rate of 84.5 kW/m^3. The pathway of heat flow in this case is a series network of material and interfacial thermal resistances associated with various components. Within the cell, these include electrodes, current collectors, separators, electrolyte, and the cell casing. Outside the cell, the aluminum casing and channel walls offer conductive resistance. Thermal spreading effects are neglected in the present analysis due to the minimal thicknesses of the aluminum casing and channel walls. Finally, convective thermal resistance is calculated based on the liquid flow rate, channel dimension, and fluid properties at the specified coolant temperature. Using this model, the steady-state temperature rise in the cell core is calculated for a specified coolant flow rate and temperature. Thermal efficiency of 95% is assumed for the cells. The radial conductive thermal resistances R_{cond} for various cell components are calculated by

$$R_{cond} = \ln\left(\frac{r_o}{r_i}\right) \times \frac{1}{2\pi h_{cell} k_{mat}} \tag{1}$$

where r_o and r_i are outer and inner radii, respectively, h_{cell} is the cell height, and k_{mat} is the thermal conductivity of the material.

The convective thermal resistance R_{conv} is calculated as follows:

$$R_{conv} = \frac{1}{h \times 2\pi R h_{cell}} \tag{2}$$

where R is the cell outer radius and h is the convective heat transfer coefficient, which can be calculated as follows:

$$h = \frac{\mathrm{Nu} \cdot k_{fluid}}{D_{hydraulic}} \tag{3}$$

where k_{fluid} is the thermal conductivity of thermal conductivity of the fluid and $D_{hydraulic}$ is the hydraulic diameter of the channel. The Nusselt number Nu is calculated based on entry length correlations [15]. In this case, the thermal entry length $x_{Th} = D \cdot 0.05 \cdot \mathrm{Re} \cdot \mathrm{Pr}$ is found to be 3.79 m, which is longer than the heat exchanger length. Thermal properties and geometric values for the different components of the cell are taken from the literature [16,17] and are listed in Table 1.

Table 1 Material and geometric properties of different components in 18650 Li-ion cell, taken from the literature [15,16]

Component	Thickness (μm)	Thermal conductivity (W/m-K)
Positive electrode	66	1.8
Negative electrode	96	1.0
Electrolyte soaked separator	50	0.35
Current collector (Cu)	35	386
Current collector (Al)	35	204

For the hybrid-propulsion system considered here, the peak battery power requirement is expected to occur at takeoff, at which point, the battery system is expected to dissipate 126 kW heat. A key goal of this analysis is to understand the effect of various design configurations on the weight of the BHAS relative to total system weight, which is a critical performance parameter for aerospace thermal management due to the large fuel consumption penalty for additional weight. A worst-case value of 39.4 °C is assumed for the air temperature.

2.1 One-Dimensional Framework Validation. The 1D thermal model is validated against a detailed 2D finite element model of a spiral-wound battery. The 2D finite element is developed in COMSOL MULTIPHYSICS®. In this model, the wound coil structure of an 18650 cell is explicitly considered. The modeled domain is shown in Fig. 2(*a*). Various layers of the 18650 cell are modeled in a spiral manner in order to simulate the actual internal geometry of the cell. Heat generated during cell discharge is specified as a volumetric source term in the governing energy conservation equation, which is the general differential equation based on energy conservation that must be solved analytically or numerically to determine the temperature field. As shown in Fig. 2, a single-electrode domain is modeled, in which the electrode domain is structured in a spiral pattern, and each successive layer of the spiral coil is separated by a thermal boundary resistance. An isotropic thermal conductivity is used for the electrode domain. An effective in-plane thermal conductivity $k_{\parallel}$ is determined from the parallel combination of the thermal resistance due to the negative and positive electrodes, the separator, and the current collectors moving in the direction along with the spiral coil, Eq. (4). In Fig. 2, the black barrier separating adjacent layers of the electrode in the spiral coil acts as a thermal resistance in the radial direction. An effective through-plane thermal conductivity $k_{\perp}$ is determined from the perpendicular combination of the thermal resistance due to battery constituents, Eq. (5).

$$k_{\parallel}=\frac{\sum k_i t_i}{\sum t_i} \tag{4}$$

$$k_{\perp}=\frac{\sum t_i}{\sum t_i/k_i} \tag{5}$$

In Eqs. (4) and (5), k and t refer to thermal conductivity and thickness of various components, respectively.

The aluminum casing is also modeled along with the channel wall, which is made of copper. Thermal contact resistance between the aluminum casing and the channel walls is neglected. A convective boundary condition on the channel wall is specified. The same heat transfer coefficient as calculated in the 1D thermal network- based model (3,000 W m^{-2} K^{-1}) is used in the 2D simulation model. The 2D geometry is discretized using a total of 118,798, 119,800, and 120,779 elements, using a uniform mesh element size, to establish mesh sensitivity, and the calculated cell center temperature for each mesh was 58.0 °C, 58.6 °C, and 58.6 °C, respectively. The mesh size choices are not established based on a specific criteria/length scale of the finest element, rather a series of incremental uniform mesh refinements is conducted. The final mesh used in the work is a uniform mesh throughout the spirally wound battery with no mesh element clustering.

Figure 2(*b*) shows a color plot of temperature distribution inside the modeled domain for a heat generation rate of 84.5 kW/m^3, corresponding to a 2C discharge rate. As expected, the maximum temperature occurs at the center of the cell. For the same heat generation and boundary conditions, the core temperature rise of an 18650 Li-ion cell as calculated from the 1D and the 2D model are 4.05 °C and 3.83 °C, respectively, at the center of the cell. In general, the two models are in good agreement. The minor deviation between the two possibly arises due to thermal spreading, which is not accounted for in the 1D model. Nevertheless, the 1D model provides a slightly more conservative estimate of temperature rise in the cell during operation, which is desirable. This analysis was conducted under steady-state conditions with a 2 C-rate discharge.

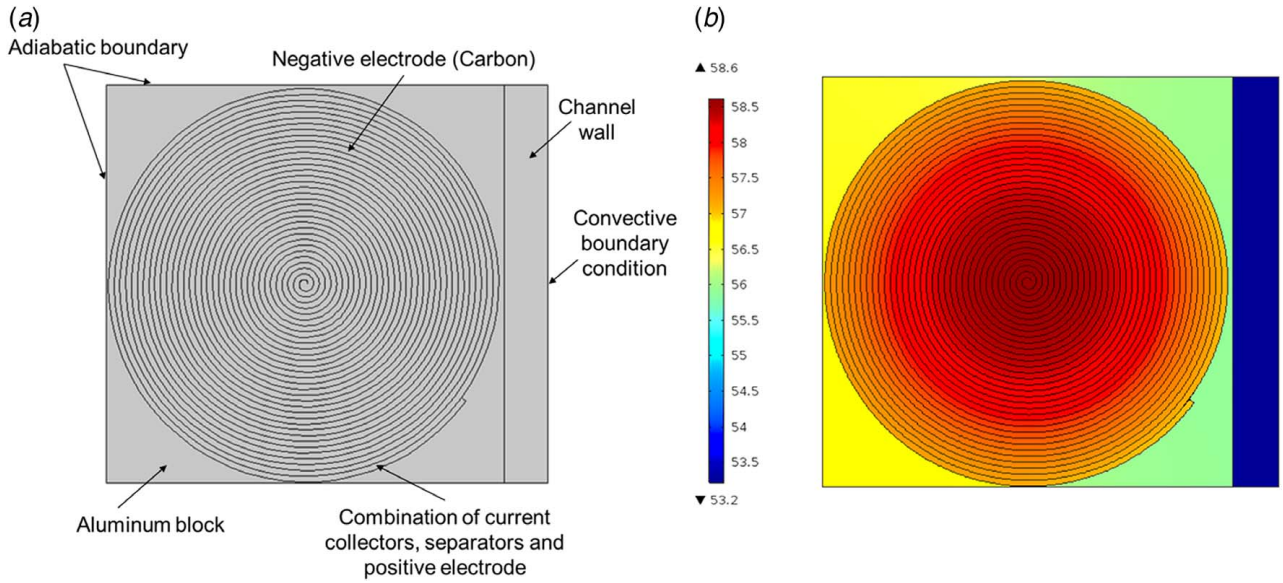

Fig. 2 2D finite element analysis modeling domain and temperature distribution in 18650 Li-ion cell

However, under transient conditions, there may be different observed temperature differences across the cell due to preferential conduction along the higher conductivity in-plane direction compared to the through-plane direction.

3 Baseline BHAS Design

The conceptual design of a baseline BHAS for the hybrid electric aircraft is adapted from the thermal management system for the battery pack of Tesla electric vehicles [18]. This specific heat acquisition system manages thermal dissipation from a 53 kW-h Li-ion battery module in a commercially available Tesla Roadster electric vehicle. Based on the Tesla automotive approach, the system runs a set of parallel battery coolant channels around the individual Li-ion cells, cooling the outside of the cylindrical cell. Incoming coolant is distributed into multiple parallel paths at the inlet plenum. Each parallel path flows across two arrays, each comprising 20 cells, and then merges with others at the outlet plenum. Each parallel path comprises five vertically stacked rectangular channels. A baseline analysis is carried out for a projected cell-level power density of 250 W-h/kg using 18650 Li-ion batteries. Figure 3 shows a schematic of the flow path and the channel distribution.

In order to derive the size and weight of the baseline BHA system, the number of cells required to meet the energy demand must be determined. The total length of the cooling channel needed is roughly equal to the number of cells times the cell diameter, while the height is equal to the cell height, for example. The Hybrid Geared Turbo Fan, Concept of Operations (hGTF CONOPS) requires 1295 kW-h energy at the low spool and 75 kW-h of energy for aircraft electric loads over a mission. At current electric machine and battery conversion efficiencies, this translates to 2029 kW-h of battery energy capacity (including 95% battery efficiency and 20% minimum state of charge). With electric machine improvements expected through current NASA-funded programs and battery improvement expected through Battery500 Consortium research, the required capacity could drop to 1681 kW-h (96% battery efficiency and 10% minimum state of charge). Regardless, the required number of cells is derived from this pack capacity requirement and the capacity of each cell. The capacity of each cell, determined by cell energy density and diameter, affects the weight of the BHA system. With the increasing cell diameter, each cell can store more energy, requiring less cells for given pack energy. With less cells, fewer cooling channels are required, reducing the weight of the BHA system. However, heat rejection per cell increases, as does the center-to-wall thermal resistance within the cell (the resistance network shown in Fig. 1). Thus, the ΔT from the cell center to the cell surface ($\Delta T_{CC\text{-}CS}$, i.e., the product of heat rejection and thermal resistance) increases, generally requiring lower coolant temperature and/or higher coolant flow rate.

An optimal cell diameter that balances heat exchanger weight and cell temperature rise may exist. In order to determine this optimal cell diameter, the maximum cell core temperature is set at 55 °C (max operating temperature beyond which permanent cell damage could occur). Thus, this temperature difference accounts for the temperature rise due to heat picked up from all cells in an array and the temperature difference from the cell center to the cell surface. The diameter of the cell is varied, and the resulting ratio of the BHA system to the total cell weight, $\Delta T_{CC\text{-}CS}$ (the cell center to the cell surface) and work required to pump the fluid, i.e., the required coolant volumetric flow rate multiplied by coolant pressure drop, are calculated. Finally, the coolant flow rate must increase to maintain a temperature difference of 5 °C between the center of the last cell in the flow network and the cooling fluid inlet temperature. The increase is required both to decrease the thermal resistance between the cell surface and the fluid (higher heat transfer coefficient with higher coolant flow and velocity) and to accept the increased heat rejection from the cells so that the coolant temperature rise from inlet to outlet is decreased. Figure 4 shows that a diameter of around 18 mm offers a reasonable compromise between these two conflicting objectives. Therefore,

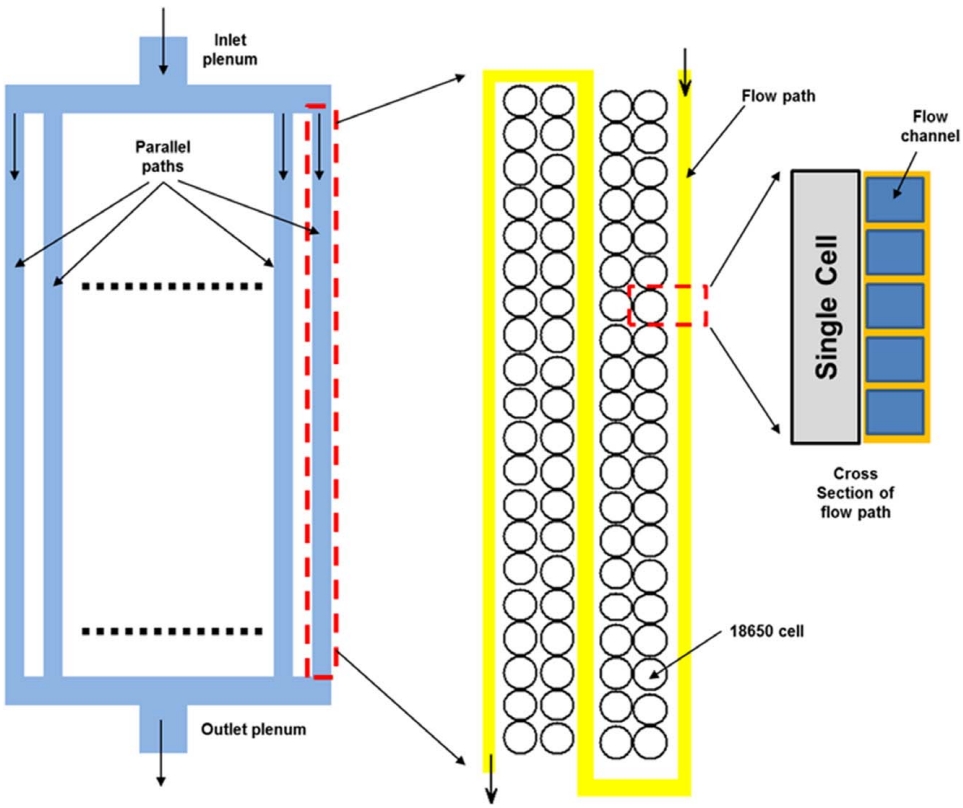

Fig. 3 Schematic of the thermal model for TESLA's BHA system

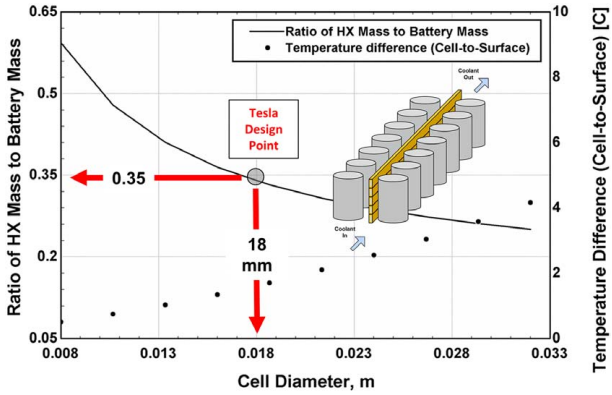

Fig. 4 Baseline (Tesla design) ratio of the BHA system to battery mass and the cell center to cell surface temperature difference as a function of cell diameter

because the Tesla battery pack uses 18650 cells, pack burden for this design is 0.36 kg/kg, and this serves as the baseline design point for this work.

Based on this early stage design analysis, the cell and BHA system specifications of a 2029 kW-h battery pack are summarized in Table 2.

4 Technology Evaluation

4.1 Evaluation Framework. Given the large number of candidate thermal management technologies that have been investigated for cooling of Li-ion cells in general, a technology evaluation framework specific to aerospace applications is critical, particularly during the early design stage where the most suitable technology for cooling of battery pack of the hybrid electric aircraft must be identified prior to the detailed design. For this purpose, a resistance network formulation shown schematically in Fig. 5 is used to model the heat transfer pathway from the center of the cell to the ultimate rejection to the coolant. Depending on the specific thermal management approach investigated, the nature of the thermal resistances in the resistance network may change. However, the typical heat transfer pathway remains the same—heat generated in the cell first passes through the various constituent materials, across contact resistances between the battery wall and a conductive medium, then through a conductive medium that connects the battery to the coolant channels, across contact resistances between the conductive medium and the channel walls, conduction through the coolant channel walls, and convection to the coolant fluid.

An energy balance between heat generated by the cells and heat removed by the coolant allows for the coolant temperature to be calculated at each node. Following this, the thermal resistance network is used to solve for the cell temperatures at each node. Equations for energy balance and heat transfer within each node are given by Eqs. (6) and (7):

$$\dot{q} = \frac{T_{cell}[i] - T_{fluid}[i]}{R_{total}[i]} = Power_{cell} = \dot{m} C_{p,l}(T_{fluid}[i] - T_{fluid}[i-1]) \tag{6}$$

$$R_{total} = R_{cell} + R_{contact} + R_{connect} + R_{contact} + R_{channel-wall} + R_{convection} \tag{7}$$

Here, T, $\dot{q}$, and R refer to temperature, heat flux, and thermal resistance, respectively. Furthermore, $\dot{m}$ and $C_{p,l}$ refer to the mass flow rate and heat capacity, respectively.

The maximum temperature in the battery configuration is constrained to stay below 55 °C, by assigning this value to the final cell node or discretization node in the coolant flow path. The coolant inlet temperature is specified to be 5 °C below the maximum cell temperature of the last cell. Therefore, the mass flow rate of the coolant is not fixed. Instead, it is iterated such that the energy balance satisfies the temperature constraints above.

4.2 Concepts Considered. The baseline BHAS uses cylindrical cells, mainly due to supply chain and modularity considerations. However, the fill required around the cylindrical cell to yield a flat surface can interface with the cooling channels and typically has a large weight. Prismatic cells are flat and can be compactly integrated with a BHA system. Due to the reduced need for fill material and increased energy storage density, BHA systems for prismatic cells are also analyzed and compared to the baseline case. Eight specific configurations with prismatic cells are considered, as described later and shown schematically in Figs. 6–8.

The first four involve outer cell cooling and are shown in Fig. 6. In the first configuration (a), conduction bars are sandwiched between cells and connected to an air-cooled pin fin heat exchanger bonded to the top and bottom edges of the cells and conductors. Air flow occurs in the out-of-plane direction.

In the second configuration (b), heat pipes are sandwiched between cells and connected to an air-cooled pin fin heat exchanger bonded to top and bottom edges of the cells and conductors. Air flow occurs in the out-of-plane direction. In each of the four configurations described earlier, the aluminum conduction bars and copper heat pipes are assumed to be 1.5 mm and 0.5 mm thick, respectively.

Figure 7 shows two additional configurations analyzed in this work. In configuration (e), shown in the first illustration in Fig. 7, equally spaced cells are immersed in FC-87, a phase-change coolant, and heat removal is due to the boiling of the coolant. In configuration (g), shown in the second illustration in Fig. 7, conduction bars are sandwiched between cells and connected to an air jet cooled plate bonded to the top and bottom edges of the cells and conductors.

The final configuration (f) of intercell cooling is shown in Fig. 8, in which, cells are sandwiched between air or liquid cooled 8 mm microchannel heat exchangers, made of Al or polyether ether ketone (PEEK).

Table 2 Specifications of the cells and BHA system of the baseline Tesla design for a 2029 kW-h battery pack

Cell		BHA system	
Mass of each cell (g)	45	Cooling channel wall thickness (mm)	1.0
Energy per cell (kW-h)	11.25	Three-pass cooling channel total length (mm)	1080
Number of cells	180,395	Number of three-pass cooling channels	12,787
Total cell weight (kg)	8056	Cooling channel weight (kg)	1140
		Weight of fill material between cells and coolant channels (kg)	1101
		Flow per channel and total flow rate (kg/s)	0.003 and 38.36
		Pack BHAS burden (BHAS weight/cell weight)	0.36

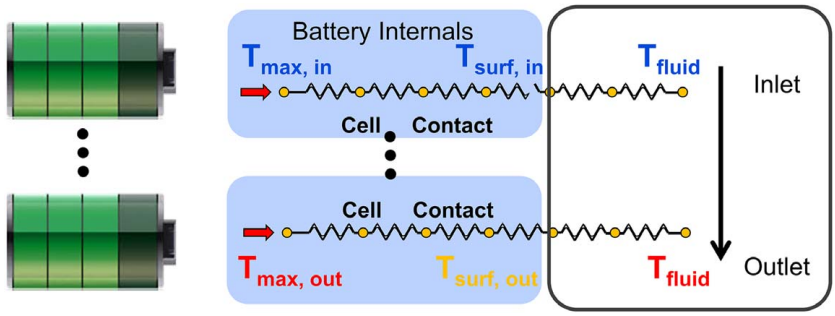

Fig. 5 Resistance network and flow path linkages used for temperature predictions

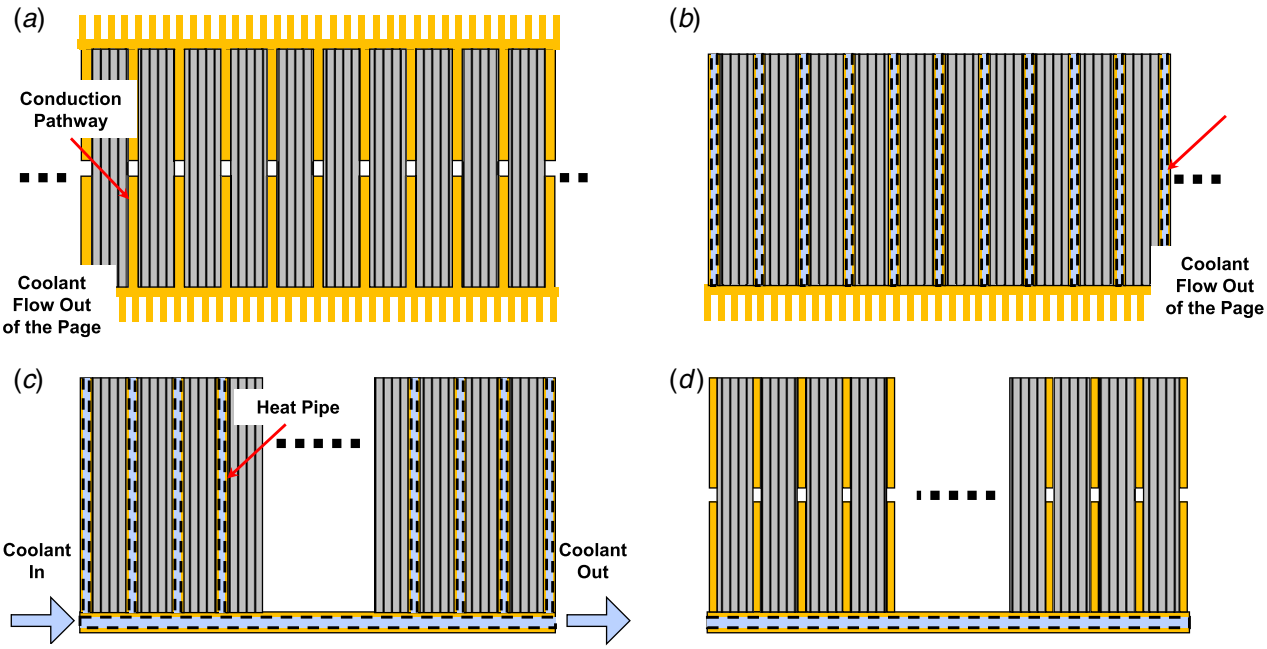

Fig. 6 Conduction plate cooling and heat pipe cooling BHA systems with air and liquid channels for ultimate heat removal

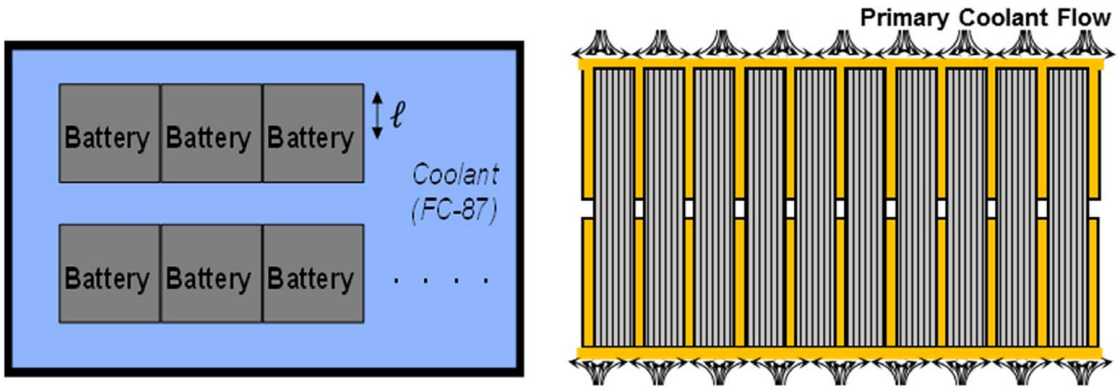

Fig. 7 (Left) Immersion cooling BHA system (e) and (right) jet air cooling BHA systems (g)

4.3 Analysis and Results. The various cooling configurations for a prismatic battery pack are analyzed to determine the optimal cell thickness, similar to the cylindrical cell analysis discussed in Sec. 4.1. As mentioned earlier, the maximum temperature in the battery pack is specified to be 55 °C. In addition, the temperature difference between the hottest cell surface in an array and the inlet coolant ($\Delta T_{CS\text{-}FI}$) is set to 5°C. Therefore, similar to the cylindrical cell analysis, the mass flow rate of the coolant is determined from energy balance considerations in order to satisfy these temperature constraints.

The cooling configurations are evaluated using three metrics—the ratio of BHA system weight to battery weight, core-to-surface

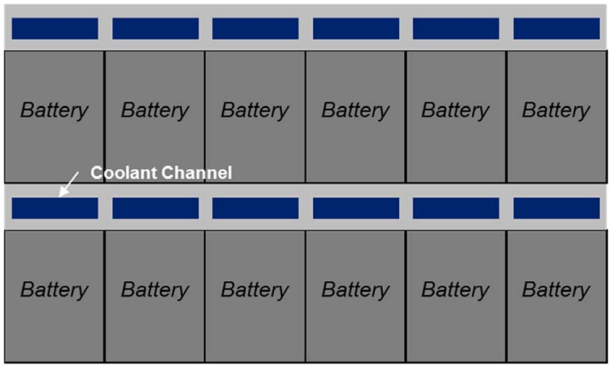

Fig. 8 Intercell cooling BHA concept (*f*)

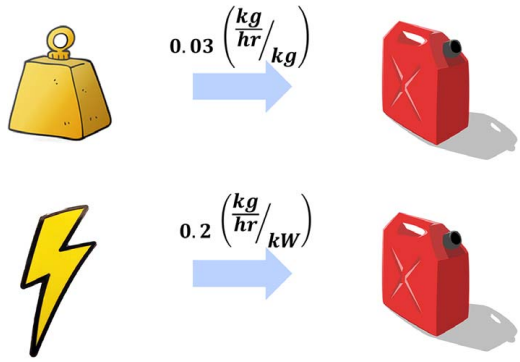

Fig. 9 Expected fuel burn penalty due to added weight and power draw from the BHA system for a single-aisle configuration

temperature difference in the cell ($\Delta T_{CC\text{-}CS}$), and the fluid pumping work ($\dot{V} \times \Delta P$) needed for the cooling, which is a function of both flowrate and pressure drop. A cell thickness is chosen in order to provide the same $\Delta T_{CC\text{-}CS}$ as the baseline. Since both weight and power translate to additional fuel burn in the context of flight, weight and fluid work metrics are combined into the single fuel burn metric through the fuel burn sensitivity model shown schematically in Fig. 9.

Figures 10–12 summarize the results of this parametric study. Figure 10 plots the ratio of heat exchanger weight and battery weight as a function of cell thickness. While all configurations outperform the baseline on mass ratio, Fig. 10 shows the heat pipe configurations (b) and (c) have the highest mass ratios, while the conduction bar configurations (a), (d), and (g) have the lowest mass ratios. Configuration (f) lies between these two extremes

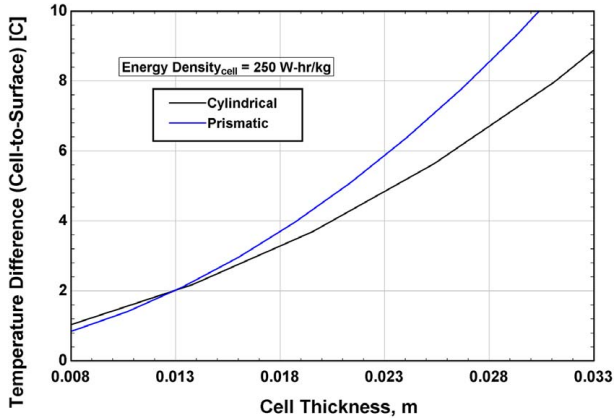

Fig. 11 Comparison of temperature difference from the cell center to the cell surface for prismatic versus cylindrical

and incur somewhat high weight due to the cooling channels covering the full surface area of each cell. Note that the curve for configuration (f) shown in Fig. 10 assumes aluminum cooling channels—the curve shifts closer to conduction bar configuration performance when the material is PEEK instead. Finally, Fig. 10 shows that configurations with air cooling offer slightly lower weight than liquid coolant configurations. Note that some of the configurations analyzed here do not have solutions across the entire cell thickness domain. For example, the curve for immersion cooling only extends up to about 10 mm because the constraint of the temperature gradient within the cell could not be maintained at greater cell thicknesses.

Figure 11 plots the maximum core-to-surface temperature difference as a function of cell thickness for both prismatic and cylindrical configurations. Figure 11 shows that the maximum $\Delta T_{CC\text{-}CS}$ is reasonably close to the baseline for the prismatic configurations at cell thickness less than about 18 mm.

Finally, Fig. 12 plots the fluid work needed as a function of cell thickness for various configurations. For comparison, performance of the baseline configuration is also plotted. Figure 12 shows that the fluid work varies widely for the BHA system configurations studied. The liquid cooled configurations (c) and (d) far outperform the air cooled and baseline configurations on fluid work by up to five orders of magnitude. This may be particularly important for aviation because additional fluid work results in increased total fuel burn. In addition, the fluid work is largely insensitive to cell thickness for all but the air jet cooling configuration.

These figures show that heat pipe configurations (b) and (c) suffer from the increased weight due to the use of copper instead of

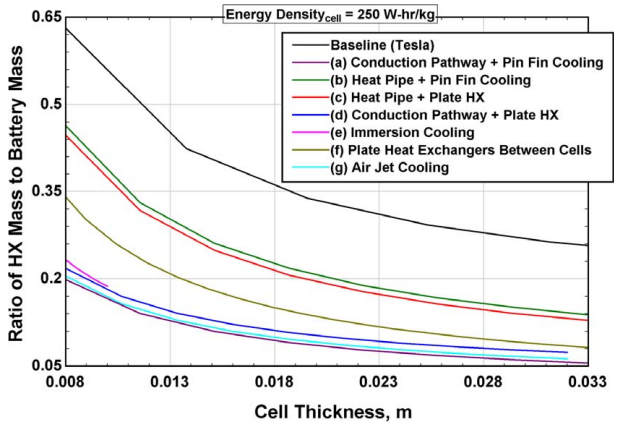

Fig. 10 Comparison of the ratio of BHA systems mass to battery mass

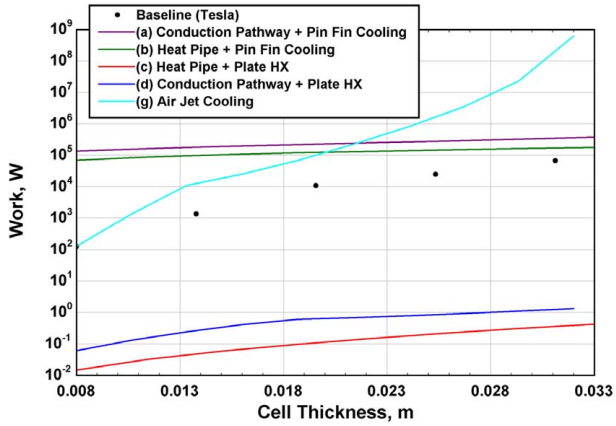

Fig. 12 Comparison of pressure drop work for BHA systems

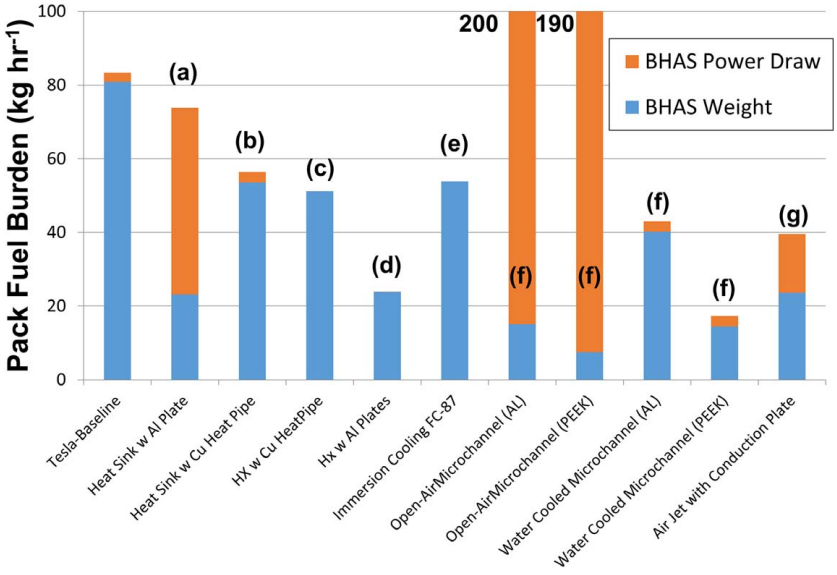

Fig. 13 BHA system compared on a fuel burn basis

aluminum, which incidentally is also a key drawback of the baseline design. However, heat pipe is very effective in minimizing temperature nonuniformity along the cell width. In addition, the use of heat pipe reduces the required coolant mass flow rate and therefore pumping power requirement.

Note that for the same temperature constraint and heat removal load, pumping power requirement for air is significantly larger than for a liquid. However, the weight penalty for using a liquid coolant is small when compared to the mass of the metal in the heat exchanger. As a result, it is expected that liquid cooling configurations (c) and (d) may outperform air cooling configurations (a) and (b).

Immersion cooling with FC-87 offers several potential benefits, but it is also limited by two significant constraints. The first is the large superheat temperature difference required for pool boiling. Further, a minimum distance is needed between two adjacent surfaces to prevent vapor lock, which in this case will have a negative impact on energy storage density. For these two reasons, immersion cooling may not be effective for an aerospace BHA system.

Based on this analysis, a cell thickness of 18 mm is chosen for the prismatic cell for comparison with the baseline cylindrical cell. All performance parameters are converted into fuel burn rate, as illustrated in Fig. 9. This cost function accounts for the fuel burn rate (kg/h) required to carry the BHA system weight and to provide power for the cooling flow.

Fuel burn of the various BHAS configurations evaluated here is presented in Fig. 13. Figure 13 shows that the air cooled options have low fuel burn associated with weight. However, with the exception of configuration (b), the large pumping power due to high flow rate and high pressure drop results in high total fuel burn associated with the power required by the BHA system. Both heat pipe configurations—liquid cooled (c) and air cooled (b)—have low pumping power due to the low heat pipe thermal resistance, but the BHAS is heavy, as discussed earlier. The water cooled microchannel PEEK variant of configuration (f), liquid cooled conduction bar configuration (d), and air jet configuration (g) with conduction bars appear to offer good overall performance. The BHA system burden for these configurations is below 15%, compared to 36% for the baseline.

5 Conclusions

This study investigates the fundamental tradeoffs involved in the design of thermal management systems for battery packs for aerospace applications. The study accounts for the challenges unique to flight and offers a framework for performance comparison and optimization of multiple candidate thermal management approaches. Based on the optimization approach, significant improvement in weight and associated fuel burn of the baseline BHA system is demonstrated. A range of thermal management approaches are evaluated to minimize the overall weight and fuel burn. Preliminary analysis shows significant potential to reduce the weight of the battery heat acquisition system by over 70%. These results may provide useful guidelines for early-stage evaluation and design of battery thermal management systems, particularly in the context of aerospace applications where multiple conflicting considerations must be carefully accounted for.

Acknowledgment

The material provided in this document is based on the work supported by the National Aeronautics and Space Administration under Contract No. NNC14CA32C. This material is partly based on the work supported by CAREER Award No. CBET-1554183 from the National Science Foundation. Any opinions, findings, and conclusions or recommendations expressed in this material are those of the author(s) and do not necessarily reflect the views of the National Aeronautics and Space Administration.

References

[1] Lents, C., Hardin, L., Rheaume, J., and Kohlman, L., 2016, "Parallel Hybrid Gas-Electric Geared Turbofan Engine Conceptual Design and Benefits Analysis," 52nd AIAA/SAE/ASEE Joint Propulsion Conference, AIAA Propulsion and Energy Forum, Salt Lake City, UT, July 25–27, pp. 1–13.

[2] Rosario, R. D., 2014, "A Future With Hybrid Electric Propulsion Systems: A NASA Perspective," https://ntrs.nasa.gov/archive/nasa/casi.ntrs.nasa.gov/20150000748.pdf, Accessed February 5, 2020.

[3] Glavaski, S., 2018, "Plug and Fly: Getting Electric Aviation Up in the Sky," https://arpa-e.energy.gov/sites/default/files/Sonja-Glavaski-Fast-Pitch-2018.pdf, Accessed February 5, 2020.

[4] Harmon, F. G., Frank, A. A., and Chattot, J.-J., 2006, "Conceptual Design and Simulation of a Small Hybrid-Electric Unmanned Aerial Vehicle," J. Aircraft, **43**(5), pp. 1490–1498.

[5] Rosero, J. A., Ortega, J. A., Aldabas, E., and Romeral, L., 2007, "Moving Towards a More Electric Aircraft," IEEE Aerosp. Electron. Syst. Mag., **22**(3), pp. 3–9.

[6] Annapragada, R., Sur, A., Mahmoudi, R., Macdonald, M., and Lents, C. E., 2018, "Hybrid Electric Aircraft Battery Heat Acquisition System," AIAA/IEEE Electric Aircraft Technologies Symposium., Cincinnati, OH, July 9–11, Paper No. AIAA 2018-4992, pp. 1–13.

[7] Shah, K., Vishwakarma, V., and Jain, A., 2016, "Measurement of Multiscale Thermal Transport Phenomena in Li-Ion Cells: A Review," ASME J. Electrochem. Energy Convers. Storage, **13**(3), p. 030801.

[8] Bandhauer, T. M., Garimella, S., and Fuller, T. F., 2011, "A Crtitical Review of Thermal Issues in Lithium-Ion Batteries," Crit. Rev. Electrochem. Solid-State Sci. Technol., **158**(3), pp. R1–R25.
[9] Esho, I., Shah, K., and Jain, A., 2018, "Measurements and Modeling to Determine the Critical Temperature for Preventing Thermal Runaway in Li-Ion Cells," Appl. Therm. Eng., **145**, pp. 287–294.
[10] An, Z., Jia, L., Ding, Y., Dang, C., and Li, X., 2017, "A Review on Lithium-Ion Power Battery Thermal Management Technologies and Thermal Safety," J. Therm. Sci., **26**(5), pp. 391–412.
[11] Chalise, D., Shah, K., Prasher, R., and Jain, A., 2018, "Conjugate Heat Transfer Analysis of Thermal Management of a Li-Ion Battery Pack," ASME J. Electrochem. Energy Convers. Storage, **15**(1), p. 011008.
[12] Vishwakarma, V., Waghela, C., Wei, Z., Prasher, R., Nagpure, S. C., Li, J., Liu, F., Daniel, C., and Jain, A., 2015, "Heat Transfer Enhancement in a Lithium-Ion Cell Through Improved Material-Level Thermal Transport," J. Power Sources, **300**, pp. 123–131.
[13] Drake, S., Wetz, D. A., Ostanek, J. K., Miller, S. P., Heinzel, J. M., and Jain, A., 2014, "Measurement of Anisotropic Thermophysical Properties of Cylindrical Li-Ion Cells," J. Power Sources, **252**, pp. 298–304.
[14] Drake, S., Wetz, D. A., Ostanek, J. K., Miller, S. P., Heinzel, J. M., and Jain, A., 2015, "Heat Generation Rate Measurement in a Li-Ion Cell at Large C-Rates Through Temperature and Heat Flux Measurements," J. Power Sources, **285**, pp. 266–273.
[15] Incropera, F. P., DeWitt, D. P., Bergman, T. L., and Levine, A. S., 2006, *Fundamentals of Heat and Mass Transfer*, 6th ed., John Wiley and Sons, New York.
[16] Guo, G., Long, B., Cheng, B., Zhou, S., Xu, P., and Cao, B., 2010, "Three-Dimensional Thermal Finite Element Modeling of Lithium-Ion Battery in Thermal Abuse Application," J. Power Sources, **195**(8), pp. 2393–2398.
[17] Chen, S. C., Wan, C. C., and Wang, Y. Y., 2005, "Thermal Analysis of Lithium-Ion Batteries," J. Power Sources, **140**(1), pp. 111–125.
[18] Adams, D. T., Berdichevsky, G., Everett, C., Hebert, A., Kohn, S., Lyons, D., Mendez, N. J., Straubel, J. B., West, D., and Simpson, A., 2007, "Battery Pack Thermal Management System," U.S. Patent No. US20090023056A1.